4

A New Method to Estimate the Temporal Fraction of Cloud Cover

Esperanza Carrasco[1], Alberto Carramiñana[1], Remy Avila[2], Leonardo J. Sánchez[3] and Irene Cruz-González[3]
[1]*Instituto Nacional de Astrofísica, Óptica y Electrónica, Puebla*
[2]*Centro de Física Aplicada y Tecnología Avanzada Universidad Nacional Autónoma de México, Santiago de Querétaro*
[3]*Instituto de Astronomía, Universidad Nacional Autónoma de México, México D.F.*
México

1. Introduction

High altitude astronomical sites are a scarce commodity with increasing demand. A thin atmosphere can make a substantial difference in the performance of scientific research instruments like millimeter-wave telescopes or water Čerenkov observatories. In our planet reaching above an altitude of 4000 m involves confronting highly adverse meteorological conditions. Sierra Negra, the site of the Large Millimeter Telescope (LMT) is exceptional in being one of the highest astronomical sites available with endurable weather conditions.

One of the most important considerations to characterize a ground-based astronomical observatory is cloud cover. Given a site, statistics of daytime cloud cover indicate the usable portion of the time for optical and near-infrared observations and bring key information for the potentiality of that site for millimeter and sub-millimeter astronomy. The relationship between diurnal and nocturnal cloudiness is strongly dependent on the location of the site (1). For several astronomical sites it has been reported (1) that the day versus night variation of the cloud cover is less than 5 %. Therefore, daytime cloud cover statistics is a useful indicator of nighttime cloud conditions.

We developed a model for the radiation that allowed us to estimate the fraction of time when the sky is clear of clouds. It consists of the computation of histograms of solar radiation values measured at the site and corrected for the zenithal angle of the Sun.

The model was applied to estimate the daytime clear fraction for Sierra Negra (2). The results obtained are consistent with values reported by other authors using satellite data (1). The same method was applied to estimate the cloud cover of San Pedro Mártir -another astronomical site (3) . The estimations of the time when the sky is clear of clouds obtained are also consistent with those reported by the same authors (1). The consistency of our results

with those obtained applying different and classical techniques shows the great potential of the method developed to estimate cloud cover from in situ measurements.

In this chapter our model will be explained. In §2 the main characteristics of solar radiation through the terrestrial atmosphere are discussed; in §3 our method to estimate the temporal fraction of cloud cover is described using radiation data of the astronomical sites Sierra Negra and San Pedro Mártir. In §4 a brief summary is presented.

2. Solar radiation through the terrestrial atmosphere

2.1 The Sun

The Sun provides energy to the Earth at an average rate of $s_\odot = 1367\,\mathrm{W/m^2}$. This value relates directly to the solar luminosity, $L_\odot = 3.84(4) \times 10^{27}$Watts, as observed at an average distance of one astronomical unit, $s_\odot = L_\odot / \left(4\pi d_\oplus^2\right)$, with $d_\oplus = 1\ UA \simeq 1.496 \times 10^{11}$ m. The value of $s_\odot$ is stable enough to be often referred as the *Solar constant*. Variations of the solar flux arise from intrinsic variations in the solar luminosity and seasonal variations of the distance between the Earth and the Sun. The eccentricity of the orbit of the Earth around the Sun, $\varepsilon_\oplus = 0.0167$, translates into minimum and maximum distances of $d_\oplus/(1 \pm \varepsilon)$, and hence a yearly modulation ($\propto \varepsilon_\oplus^2$) of $\pm 3.3\%$ in the solar flux over the year. Given a location on the Earth, this modulation is smaller than seasonal variations due to the changes of the apparent trajectory of the Sun in the sky, originated by the inclination of the Earth spin axis relative to the ecliptic. Intrinsic variations of the solar flux due to changes in luminosity, some tentatively related to the 11-year solar activity cycle, are very low, of the order of 0.1%.

The solar radiation is distributed along the infrared to ultraviolet regions of the electromagnetic spectrum. This distribution is shown in terms of apparent magnitudes m_ν in standard spectral bands, from the ultraviolet (U) to the infrared (IHJK), in Table 1 and plotted in Fig. 1. The conversion into energy flux F_ν is made through the standard formula:

$$F_\nu = F_\nu^0\, 10^{-0.4 m_\nu}. \tag{1}$$

A comparison of the solar spectrum with a blackbody spectrum can be made defining three temperature measures: the effective temperature; the color temperature; and the brightness temperature:

- the effective temperature T_e is given by the integrated flux F and the angular size of the radiation source, $F = \sigma T_e^4 \delta\theta^2$, with $\delta\theta$ the apparent radius and σ the Stefan Boltzmann constant. For the Sun $T_e \simeq 5770$ K, which corresponds to a maximum emission at a wavelength $\lambda \simeq 0.5\,\mu$m.
- the color temperature is calculated through the best blackbody fit of the spectrum. Fig. 1 shows a blackbody fit to F_ν of the form $A\nu^3/(e^{\nu/\nu_c} - 1)$, with best fit parameters

$$A = 1.166 \times 10^{-9} \mathrm{erg\,cm^{-2}s^{-1}}, \quad \text{and} \quad \nu_c = 1.167 \times 10^{14}\,\mathrm{Hz}, \tag{2}$$

  which result in a color temperature $T_{col} \simeq 5600\,\mathrm{K}$. As observed in the plot, a blackbody is a fair fit of the spectral distribution of the solar flux.
- the third temperature indicator of solar conditions is the brightness temperature, defined monocromatically by $I_\nu = B_\nu(T_b)$. It is nearest to the effective temperature in the I band, $\lambda = 0.9\,\mu$m.

Band	Magnitude	λ (μm)	$\Delta\lambda$ (μm)	F_ν^0 Jy	F_ν (10^{-12}W m^{-2}Hz^{-1})	$F_\nu\Delta\nu$ (W m^{-2})
U	−26.03	0.360	0.068	1880	0.485	76.
B	−26.14	0.440	0.098	4650	1.329	202.
V	−26.78	0.550	0.089	3950	2.035	179.
R	−27.12	0.700	0.22	2870	2.022	272.
I	−27.48	0.900	0.24	2240	2.199	195.
J	−27.93	1.26	0.20	1603	2.382	90.
H	−28.26	1.60	0.36	1075	2.165	91.
K	−28.30	2.22	0.52	667	1.394	44.

Table 1. Apparent magnitudes of the Sun in different bands and its conversion into energy fluxes. The integrated sum over bands gives 1150 W/m^2. The magnitudes are from (4).

The radiation we observe from the Sun and the sky is determined by radiation processes occurring in the air, on the ground and on the clouds. This is revised in the following subsections.

2.2 The terrestrial atmosphere

The atmosphere of the Earth is composed of a mixture of gases dominated by molecular nitrogen and oxygen, N_2 and O_2. It can be modeled as an ideal gas of molecular mass $\mu \simeq 29$ in local thermodynamical equilibrium under hydrostatic equilibrium in a gravity field g, thus following

$$P = \frac{\rho kT}{\mu m_H}, \quad \frac{dP}{dz} = -g\rho\,. \tag{3}$$

The last expression assumes a plane parallel atmosphere, a good approximation when the atmosphere is a layer much thinner than the radius of the planet, as in the Earth. These two equations are insufficient to solve for the three unknowns $\{\rho(z), P(z), T(z)\}$, and a third equation containing the thermodynamical behavior of the gas is needed to close the problem. The simplest atmosphere solutions are for an isothermal gas, $T =$ constant, or an adiabatic gas, $P \propto \rho^\gamma$, where γ is the ratio of specific heat capacities.

- Solving equations 3 for an **isothermal gas** gives an exponential structured atmosphere,

$$T(z) = T\,, \quad P(z) = P_0 e^{-z/H}\,, \quad \rho(z) = \rho_0 e^{-z/H}\,, \tag{4}$$

  of characteristic height scale $H = kT/\mu m_H g$. For Earth atmosphere, $\mu = 28.9644$, we get $H \simeq 8781.5$m at $T = 300$ K and $H \simeq 7171.6$m at $T = 245$ K.

- Using **adiabatic cooling** to equations 3 results in a constant temperature gradient,

$$\frac{dT}{dz} = -\frac{(\gamma-1)}{\gamma}\frac{T_0}{H}\,,$$

  with H the isothermal temperature height and T_0 the ground temperature. The adiabatic temperature gradient for $\gamma = 1.4$, nominal value for a diatomic molecular classical ideal gas, is $dT/dz = -9.8$ K/km.

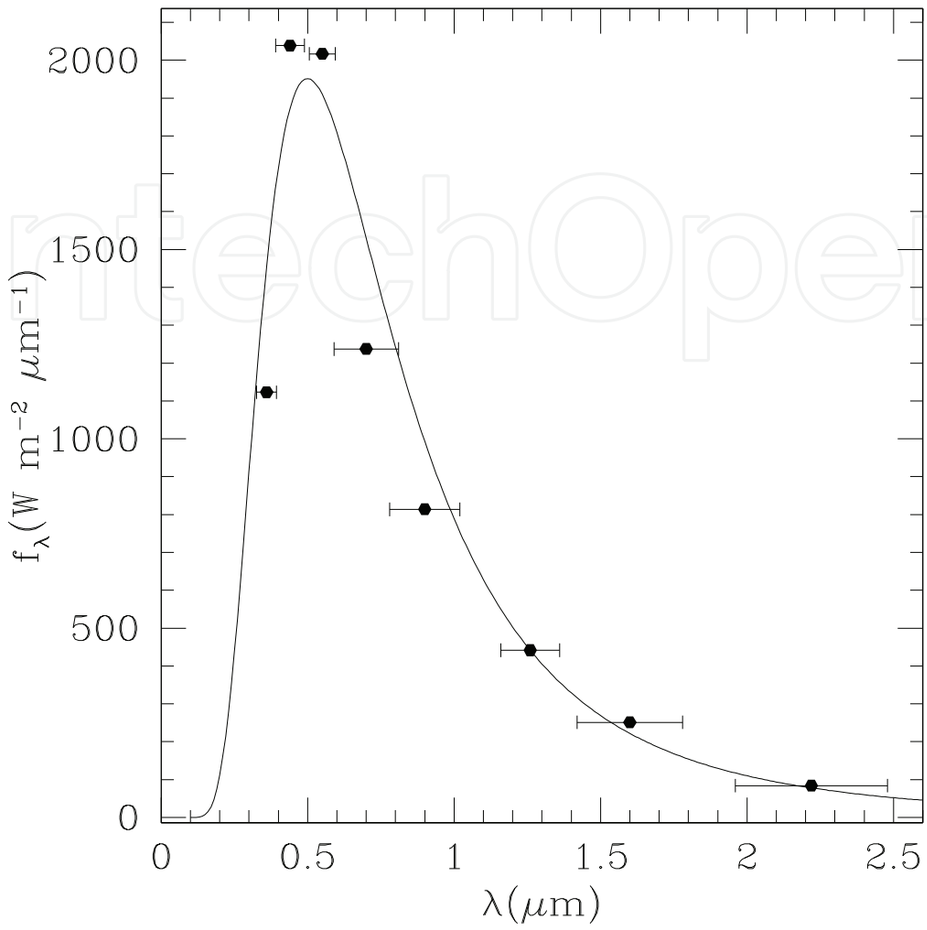

Fig. 1. Solar spectrum and blackbody fit with color temperature $T_c = 5600$ K.

A proper atmospheric solution should consider the transfer of radiation. Still, approximate solutions do provide a fair description of the terrestrial atmosphere. A still relatively simple but more precise description of the Earth's atmosphere is given by the "standard atmosphere" model, which incorporates thermodynamics through defining layers of constant temperature and constant temperature gradient. This is shown in table 2, where boundary conditions refer to the base of the atmosphere, rather than its upper edge. Note that 99 % of the atmosphere is contained in the inner 30 km. The troposphere, which constitutes $\sim$ 80 % of the atmosphere, has an structure analog to adiabatic,

$$T(z) = T_0 - \theta z\,, \quad P(z) = P_0\,(1 - \theta z/T_0)^{\alpha}\,, \quad \rho(z) = \rho_0\,(1 - \theta z/T_0)^{\alpha - 1}\,, \tag{5}$$

but with a lower temperature gradient, $\theta = -6.5$ K/km, and $\alpha = \mu m_{Hg}/k\theta \simeq 5.256$. The weather in Sierra Negra, the high altitude site of the γ-ray observatory HAWC[1] and of the LMT, has been monitored since late 2000. We found its meteorological variables to conform very closely with a standard atmosphere with $T_0 = 304$ K an adequate boundary value, fitting $P(4.1\text{ km}) \simeq 625.6$ mbar at HAWC, and $P(4.58\text{ km}) \simeq 569.5$ mbar at LMT (2). One of the

[1] High Altitude Water Čerenkov.

Capa	z_{g0} (km)	z_0 (km)	dT/dz K/km	T_0 °C	P_0 Pa
Troposphere	0	0.000	−6.5	+15.0	101 325
Tropopause	11	11.019	0.0	−56.5	22 632
Stratosphere (I)	20	20.063	+1.0	−56.5	5 475
Stratosphere (II)	32	32.162	+2.8	−44.5	868
Stratopause	47	47.350	0.0	−2.5	111
Mesosphere (I)	51	51.413	−2.8	−2.5	67
Mesosfera (II)	71	71.802	−2.0	−58.5	4
Mesopause	84.852	86.000	−−	−86.2	0.37

Table 2. Layers defining the International Standard Atmosphere. z_{g0} y z_0 are the geopotential and geometric heights, respectively, at the base of the layer.

ongoing projects at the Sierra Negra site is the simultaneous measurements of meteorological variables, and hence their gradients, in these two locations.

2.3 The transfer of solar radiation through the atmosphere

One of the most important features of the terrestrial atmosphere is its transparency to visible light, while being opaque to infrared radiation. As a consequence, most of the solar radiation reaches the ground, where it is thermalized and re-emitted as infrared radiation, which is trapped by atmospheric molecules, raising Earth's temperature above its direct equilibrium temperature. This is the basic scenario of our atmosphere; in practice this is complicated by scattering due to small particles suspended in the air, the presence of clouds, the local properties of the ground and the sea, and the non static conditions in the atmosphere (winds) and the sea (currents).

In the absence of an atmosphere, the temperature on a location where the Sun is observed with an angle $\theta_\odot$ would be given by the equilibrium condition

$$(1-a)s_\odot \cos\theta_\odot = \pi\sigma T^4, \tag{6}$$

where a represent the albedo, or fraction of the radiation reflected by the surface, and the factor π results from integrating the re-emitted radiation ($\propto \cos\theta$) over half a sphere. For an albedo $a = 0.3$, the temperature is $T \simeq 270\ \cos\theta_\odot^{1/4}$ K. The radiation emitted by the ground will be emitted in the infrared, at wavelengths of the order of 10 μm. The resulting simplification is that radiation in the atmosphere can be treated in terms of two separated components, one in the visible ($\lambda \simeq 0.5\,\mu$m) and the other in the infrared ($\lambda \simeq 10\,\mu$m).

A refinement of the previous calculation can be made assuming a *grey* atmosphere, where the term grey indicates the assumption that its radiation properties are independent of the wavelength, at least on a given spectral window. If we now assume the atmosphere absorbs 10 % of the visible light and 80 % of the infrared radiation originated on the ground, we infer that just above 60 % of the solar radiation is trapped by the atmosphere, which acquires a temperature T_a given by the energy density of the radiation captured,

$$u = aT_a^4 = \eta s_\odot / c \quad \Rightarrow T \simeq 245\,\text{K}, \tag{7}$$

with $\eta = 0.604$ and c the speed of light. As seen in the previous subsection the atmosphere is not an homogeneous layer, although most of it can be described as in local thermodynamical equilibrium, with the temperature scale $T(z)$ defined in table 2. The implicit assumption is that radiation absorption and emission rates are nearly equal locally. Although they are less abundant than N_2 and O_2, molecules like water (H_2O), carbon dioxide (CO_2) and methane (CH_4) play important roles in atmospheric radiation transfer processes. Their molecular spectra are rich in electronic, vibrational and rotational transitions. The vibrational components are important in the infrared while the rotational transitions dominate in microwaves.

Relevant to this work are the optical properties of the atmosphere. On the one hand, processes occurring in transparent air and on the other hand, the brightness of clouds. Aerosol particles suspended in the air scatter light, with preferential selection of shorter wavelengths. This process is described in terms of Rayleigh scattering, for which the cross section can be roughly written as $\sigma \approx 5.3 \times 10^{-31}\,\mathrm{m}^{-2}\,(\lambda/532\,\mathrm{nm})^{-4}$. The integration of the hydrostatic equilibrium equation (3) shows that the column density of the atmosphere is given by $\mathcal{N} = P/\mu m_{Hg} \simeq 2.1 \times 10^{29}\,m^3$, and a probability $\mathcal{N}\sigma \approx 0.1$ of absorbing a 532 nm photon in one atmosphere, assuming (wrongly) that the density of aerosol particles is proportional to that of air everywhere in the atmosphere. Taking as a benchmark $\lambda = 0.5\,\mathrm{nm}$, where the solar emission is maximum, the visible emission of the atmosphere downwards due to scattering amounts to 5 % of the solar flux distributed over an effective solid angle of π steradians, equivalent to 4.3 mag/arcsec^2. This means that even if the direct solar radiation were obstructed, an omnidirectional detector of visible radiation would measure a flux $\sim 0.05 s_\odot$. The fact that Rayleigh scattering is a process whose importance increases at short wavelengths is well known to be the origin of the blue color of diurnal sky.

The most common situation in which direct solar radiation is obstructed is cloudy weather. In cloudy conditions solar light is scatter and reflected by water particles suspended in the clouds. Without entering in details, one can see that a sizable fraction of solar radiation scattered by the clouds does reach the ground. This amount does depend on the actual conditions, but will add to the 5 % grossly estimated to arise from blue sky itself. The results of the studies presented below put the integrated emission of cloudy skies at about 20 % of $s_\odot$.

3. A method to estimate the temporal fraction of cloud cover

3.1 Introduction

In this section a new method to estimate the temporal fraction of cloud cover, based in solar radiation measurements in situ, will be described. The data are compared with the radiation expected given the coordinates of the site and hence the position of the Sun in the sky. It will be illustrated by using real solar radiation data obtained at two astronomical sites: Sierra Negra and San Pedro Mártir (SPM), both in Mexico. First, a brief introduction to the sites and the data sets will be presented. In the next section the solar modulation is explained. In the following two sections the results obtained for Sierra Negra and the statistics of clear time are described. In the two subsequent sections an additional example of the method applied to SPM and the statistics of clear time are discussed. In this case, the model proved to be sensitive enough to determine the presence of other atmospheric phenomena.

Sierra Negra, also known as Tliltepetl, is a 4580 m altitude volcano inside the Parque Nacional Pico de Orizaba, a national park named after the highest mountain of Mexico. With an altitude of 5610 m Pico de Orizaba,[2] also known as Citlaltepetl, is one of the seven most prominent peaks in the world, where prominent is related with the dominance of the mountain over the region. These two peaks are located at the edge of the Mexican plateau which drops at the East to reach the Gulf of Mexico at about 100 km distance, as shown on Fig. 2. Sierra Negra is the site of the LMT, a 50 m antenna for astronomical observations in the 0.8-3 millimeter range. LMT is the largest single-dish millimeter telescope in the world. Its performance depends critically on the amount of water absorbing molecules, mainly H_2O in the atmosphere. The top of Sierra Negra has the coordinates: 97° 18′ 51.7″ longitude West, and 18° 59′ 08.4″ latitude North. The development of the LMT site led to the installation of further scientific facilities benefiting from its strategic location and basic infrastructure like a solar neutron telescope and cosmic ray detectors, among others. In July 2007 the base of Sierra Negra, about 500 m below the summit, was chosen as the site of HAWC observatory, a $\sim$ 22000 m^2 water Čerenkov observatory for mapping and surveying the high energy γ-ray sky. The HAWC detector incorporates the atmosphere, where particle cascades occur.

Fig. 2. Map of Mexico indicating the locations of Sierra Negra site at the East and San Pedro Mártir at the North West [from Conabio site: www.conabio.gob.mx].

The data presented here were acquired with a Texas Electronics weather station. The radiation sensor was made of a solar panel inside a glass dome. The data are output as time ordered energy fluxes in units of W/m^2. The nominal range is up to 1400 W/m^2 with a resolution of 1 W/m^2 and 5 % accuracy.

The solar radiation data span from April 12, 2002 to March 13, 2008, completing a sample of 990770 minutes. The effective data coverage was 62 %. Coverage was 73 % in 2002, decreases towards 2004, with a 44 % and increases to 81 % in 2005 and 2006. The majority of the data were taken with 1 or 5 minutes sampling. The weather of the site is influenced by the dry weather of the high altitude central Mexican plateau and humid conditions coming from the Gulf of Mexico. Given the weather conditions the data points were divided in two samples:

[2] Instituto Nacional de Estadística, Geografía e Informática (INEGI) official figure.

the *dry season* is the 181 day period from November 1st to April 30; the *wet season* goes from May 1st to October 31st, covering 184 days.

The SPM observatory is located at 31°02′39″ latitude North , 115°27′49″ longitude West and at an altitude of 2830 m, inside the Parque Nacional Sierra de San Pedro Mártir. SPM is ∼65 km E of the Pacific Coast and ∼55 km W to the Gulf of California, as shown in Fig. 2. The largest telescope at the site is an optical 2.1-m Ritchey-Chrétien, operational since 1981. Astroclimatological characterization studies at SPM are reviewed in (5). Other aspects of the site characterization have been reported by several authors e.g. (7; 8). Nevertheless, the first study on the radiation data measured in situ was done by Carrasco and collaborators (3). The data were recorded by the Thirty Meter Telescope (TMT) site-testing team from 2004 to 2008. See (9) for an overview of the TMT project and its main results.

The data presented here consist of records of solar radiation energy fluxes in units of Wm^{-2} acquired with an Monitor automatic weather station (9). The sensor has a spectral response between 400 and 950 nm with an accuracy of 5 %, according to the vendor. The data span from 2005 January 12 to 2008 August 8, with a sampling time of 2 minutes and a 67 % effective coverage of the 3.6 year sample; data exist for 973 out of 1316 days. The complete sample contains 596580 min out of 899520 possible; coverage was 59 % for 2005 and increased to 78 % towards the end of the campaign, in 2008.

3.2 Solar modulation

The method to estimate the temporal fraction of cloud coverage is based on computing the ratio between the expected amount of radiation and that observed. We safely assume that, at least under clear conditions, radiation directly received from the Sun is dominant. This is a term of the form $s_\odot \cos\theta_\odot$, where $\theta_\odot$ is the zenith angle of the Sun as observed from the site under study. The modulation term is removed by simply dividing by $\cos\theta_\odot$. To compute the local zenith angle as a function of time, consider a coordinate system centered on Earth with the $\hat{z}$ axis oriented perpendicular to the ecliptic. By definition, the position of the Sun in this system is restricted to the $x-y$ plane, and is given by $d_\oplus \hat{r}_\odot$, with the direction to the Sun given by the unitary vector

$$\hat{r}_\odot = -\hat{x}\cos(\omega_a t) - \hat{y}\sin(\omega_a t)\,, \tag{8}$$

where $\omega_a = 2\pi/\mathrm{year}$ is the angular frequency associated to the yearly modulation. Given a location on Earth of geographical latitude b, the zenith is in the direction given by the unitary vector

$$\hat{n} = -\hat{z}_e \sin b + (\hat{x}_e \cos(\omega_s t) + \hat{y}_e \sin(\omega_s t))\cos b, \tag{9}$$

where $\omega_s = \omega_a + \omega_d = 2\pi/\mathrm{yr} + 2\pi/\mathrm{day}$, and

$$\hat{x}_e = \hat{x}\,, \quad \hat{y}_e = \hat{y}\cos\imath - \hat{z}\sin\imath\,, \quad \hat{z}_e = \hat{y}\sin\imath + \hat{z}\cos\imath, \tag{10}$$

with $\imath$ the inclination angle of the Earth axis relative to the $\hat{z}$, the unitary vector normal to the ecliptic plane. With these relations in hand, it follows that the zenith angle of the Sun is given by $\cos\theta_\odot = -\hat{n}\cdot\hat{r}_\odot$. Equations 8 and 9 assume $t = 0$ corresponds to the time of equinox, rather than the beginning of the civil year.

These equations were used to generate solar zenith angles for all years covered by the data. Before the actual data analysis, we verified the proper functioning of the related software, both

for Sierra Negra and for San Pedro Mártir. The comparison, shown in Figs. 3 and 4, gives an insight on the differences between sites inside or ouside the tropics: Sierra Negra, at $b \simeq 19°$ is located three degrees south of the tropic of Cancer, while San Pedro Mártir, located in the Baja California at $b \simeq 31°$N is at a moderately northern location. Fig. 3 shows the daily behavior of $\cos\theta_\odot$ for both sites, with summer months displayed in red and winter months in blue. It is clear that the range of values of $\cos\theta_\odot$ at time of culmination, or simply noon, is larger for San Pedro, going below 0.6 is winter, while these always reach at least 0.7 in Sierra Negra. The effect of latitude is more marked in the behavior of the values of $\theta_\odot$ near noon through the year (fig. 4). Due to its closeness to the equator, the Sun reaches the zenith twice a year at Sierra Negra, while never getting $\theta_\odot < 8°$ for San Pedro Mártir. One can calculate analytically the times of the two passage of the Sun through the zenith, which are given by

$$\cos\phi_\pm = \sin b / \sin\imath,$$

where $t = 0$ is the time of summer solstice and $\phi_\pm$ corresponds to ± 35.643 days, or passages through the zenitn on the 17^{th} of May and on the 26^{th} of July, in concordance with Fig. 4.

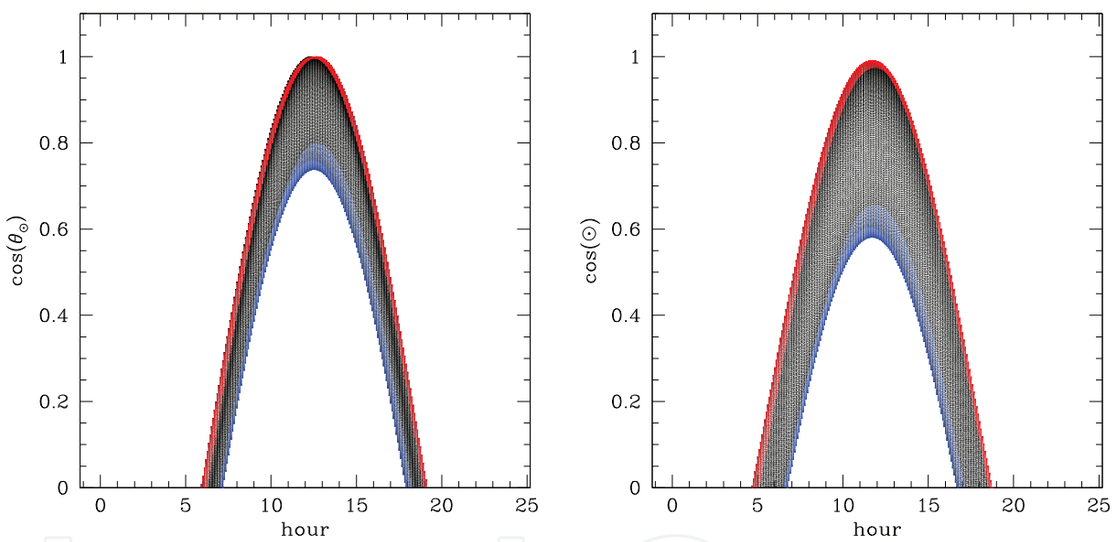

Fig. 3. Cosine of the solar zenith angles as a function of time of day for Sierra Negra (left) and San Pedro Mártir (right). Red color indicates data for June and July while blue indicates December and January. The higher elevation of the Sun as seen from Sierra Negra can be appreciated.

A direct representation of the radiation data can be seen in Fig.5, where the solar radiation is plotted *vs.* the cosine of the Sun zenith angle, $\cos\theta_\odot$. The red line corresponds to the *Solar constant* $s_\odot \times \cos\theta_\odot$. On the left side are the data corresponding to Sierra Negra while on the right side are those to SPM. The dots above the red line are spurious data as the sensor can not received more energy than that provided by the Sun to the Earth, given by $s_\odot$. Note that for Sierra Negra there is a points concentration below the red line corresponding to clear conditions i.e. the radiation measured at the site is very close to that expected. The same effect is more pronounced in the case of SPM. The latter means, as will be shown, that SPM has a larger fraction of clear time.

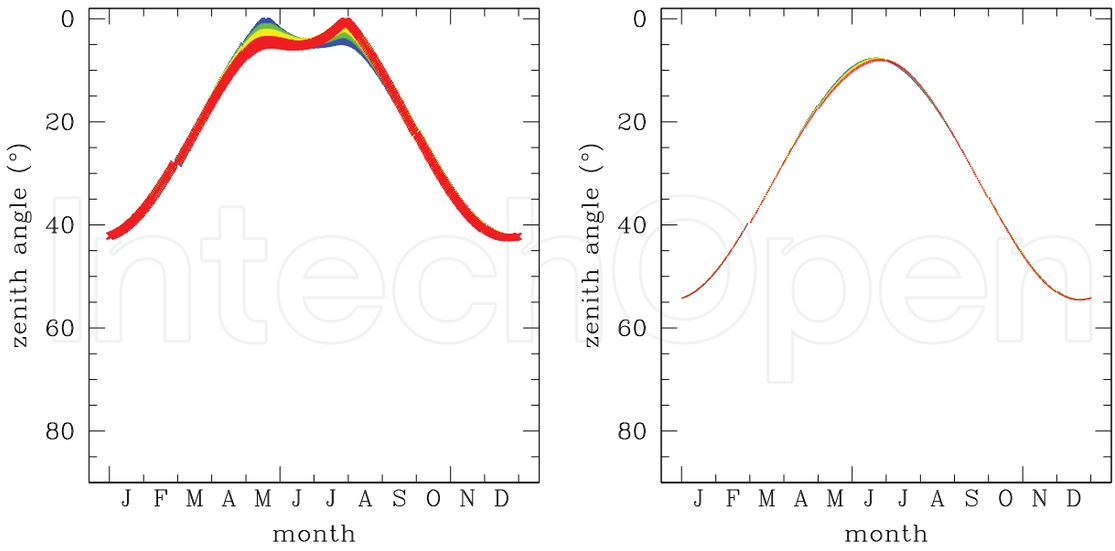

Fig. 4. Minimum zenith angle for the Sun as seen from Sierra Negra (left) and San Pedro Mártir (right). Data shown are for four 10 minute windows at or close to the local time of culmination, or solar noon. The Sun reaches the zenith ($\theta_\odot = 0°$) twice a year in Sierra Negra, while ranging from 55° to 7° at San Pedro.

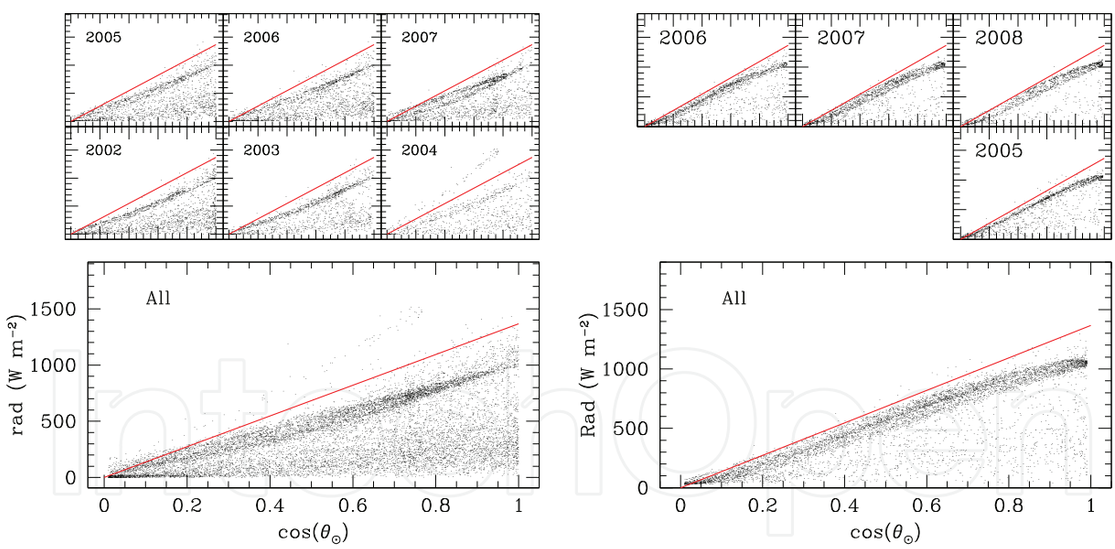

Fig. 5. Solar power versus $\cos\theta_\odot$ global and per year. The red line corresponds to $s_\odot \times \cos\theta_\odot$. Left: for Sierra Negra. Right: for San Pedro Mártir

3.3 The histogram of $\psi(t)$ for Sierra Negra

The radiation flux at ground level is considered, to first approximation, to be given by the *Solar constant* $s_\odot$, modulated by the zenith angle of the Sun and a time variable attenuation factor $\psi(t)$. Knowing the position of the Sun at the site as a function of time, we can estimate

the variable ψ, given as

$$\psi(t) = \frac{F(t)}{s_\odot \cos\theta_\odot}\,. \tag{11}$$

where $F(t)$ is the radiation measured at the site and $\theta_\odot$ is the zenith angle of the Sun. $\psi(t)$ is a time variable factor, nominally below unity, which accounts for the instrumental response (presumed constant), the atmospheric extinction on site and the effects of the cloud coverage.

Knowing the site latitude, the modulation factor $\cos\theta_\odot$ was computed as a function of day, month and local time, minute per minute to study the behavior of the variable ψ and to obtain its distribution. The term z is referred as the airmass, defined as $z = \sec\theta_\odot$; thus $z < 2$ is equivalent to $\theta_\odot < 60°$. Most astronomical observations are carry out at this airmass interval.

The histogram of values of ψ showed a bimodal distribution composed by a broad component for low values of ψ and a narrow peak $\psi \lesssim 1$, as shown in Fig. 6. The narrow component is interpreted as due to direct sunshine while the broad component is originated when solar radiation is partially absorbed by clouds; we then use the relative ratio of these two components to quantify the “clear weather fraction".

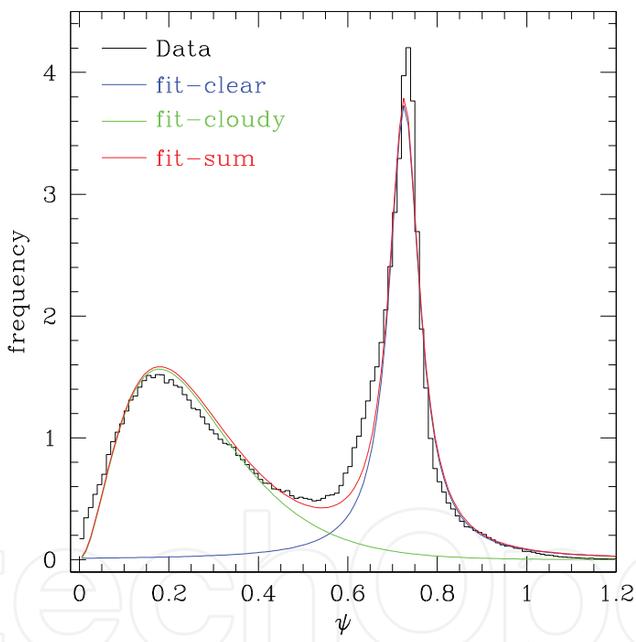

Fig. 6. The distribution of the solar flux divided by the nominal solar flux at the top of the atmosphere, $s_\odot \cos\theta_\odot(t)$, for Sierra Negra. The distribution of the complete sample shows a bimodal behaviour which can be reproduced by a two component fit, shown in solid lines.

The histogram of ψ values can be reproduced by a two component fit. The functional form of the best fit is given by,

$$f(\psi) = A\psi^2 e^{-\beta\psi} + \frac{B}{1 + [(\psi - \psi_0)/\Delta\psi]^2}. \tag{12}$$

The first term on the right hand side is a χ^2 function with six degrees of freedom. It is interpreted as the cloud-cover part of the data, with its integral being the fraction of

cloud-covered time. The second term, a Lorentzian function with centre ψ_0 and width $\Delta\psi$, represents the cloud-clear part of the data. A and B provide the normalization and relative weights of both components; β is related to the width and centre of the broad peak. In the appendix the details of the calculation of the fit parameters, including the errors, are discussed.

In Fig. 6 the distribution of ψ for the whole data set is shown in black with the double component fit in red. The first component of the fit corresponding to the cloud cover part of the data is shown in blue while the second one, corresponding to the clear part of the data is shown in green. This bimodal distribution, with a first maximum at around $\psi \sim 0.2$ and a narrow peak at $\psi \sim 0.75$, has a minimum around $\psi \sim 0.55$.

Fig. 7 presents the distribution of ψ for the dry and for the wet seasons. Clearly, in both cases the distribution of ψ is also bimodal. For the dry months when the sky is mostly clear of clouds the narrow peak is higher. In contrast, during the wet season when more clouds are present, the broad peak is more pronounced. Note that, in both cases, the fit given by Eq. 12 reproduces very well the observational data.

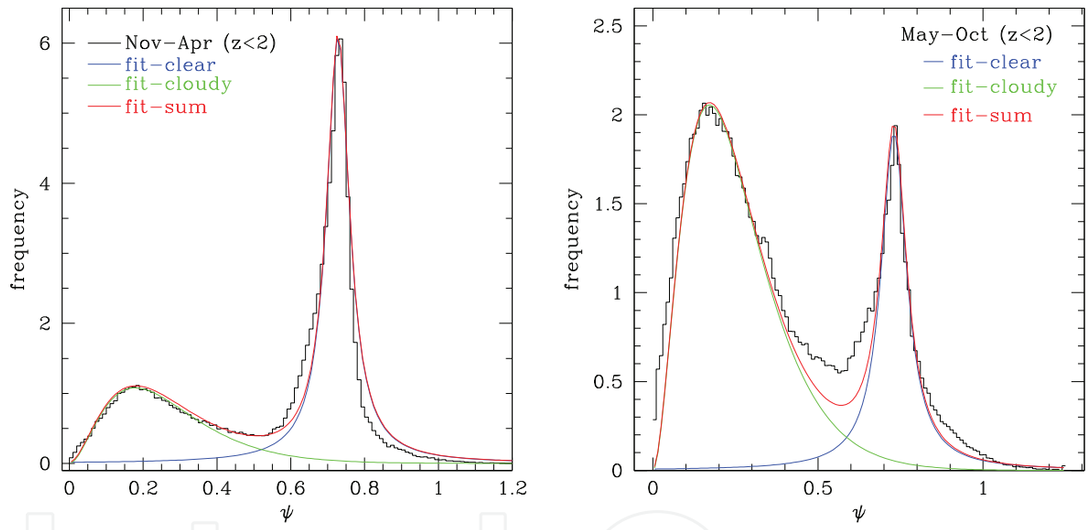

Fig. 7. The distribution of the solar flux divided by the nominal solar flux at the top of the atmosphere, $s_\odot \cos\theta_\odot(t)$, for Sierra Negra. Left: for the dry season. Right: for the wet season. In both cases, the bimodal distribution is well reproduced by a two component fit, show in solid lines.

The data were separated with $\psi \leq \psi_{min}$ as cloudy weather and data with $\psi > \psi_{min}$ as clear weather. ψ_{min} corresponds to the intersection of the two components of the function fitted to the distribution of all the data points. The fraction of clear time f(clear), was computed as clear/(clear+cloudy).

From the global distribution, a clear fraction for the site of 48.4 %, was obtained. This results is consistent with values reported by other authors (1). The authors surveyed cloud cover and water vapor conditions for different sites using observations from the International Satellite Cloud Climatology Project (ISCCP) for the California Extremely Large Telescope (CELT) project. The study period is of 58 months between July 1993 to December 1999 using

a methodology that had been tested and successfully applied in previous studies. For Sierra Negra they measured a clear fraction for nighttime of 47 %. They conclude that the day versus night variation of cloud cover is less than 5 %, being clearer at night. Therefore, the results obtained with the method presented here are consistent within 6.4 % with those obtained via a totally independent technique.

3.4 Statistics of clear time for Sierra Negra

The method described above also allow to calculate the statistics of the clear time f(clear). For completness the analysis in this section includes data with airmass less than 10. The fraction of clear time f(clear) was computed for every hour of data. The distribution of the hourly clear fraction is shown in Fig. 8 for the dry (left) and wet (right) seasons. The histograms have a strong modulation. If we consider the semester between November and April $f(\text{clear}) = 1$ has 37.4 % of the data while the $f(\text{clear}) = 0$ peak has 9.0 % of the data. This means that 37.4 % of the time the sky is clear of clouds and 9.0 % of the time the sky is cloudy. During the complementary wet months the $f(\text{clear}) = 1$ peak contains 11.4 % of the data while $f(\text{clear}) = 0$ has 32.5 % of the data. Intermediate conditions prevail around 55 % of the time in both semesters. From the f(clear) histogram of the whole data (not shown) 20.3 % of the hours have $f(\text{clear}) = 0$, while 25.0 % have $f(\text{clear}) = 1$; the remaining have intermediate values.

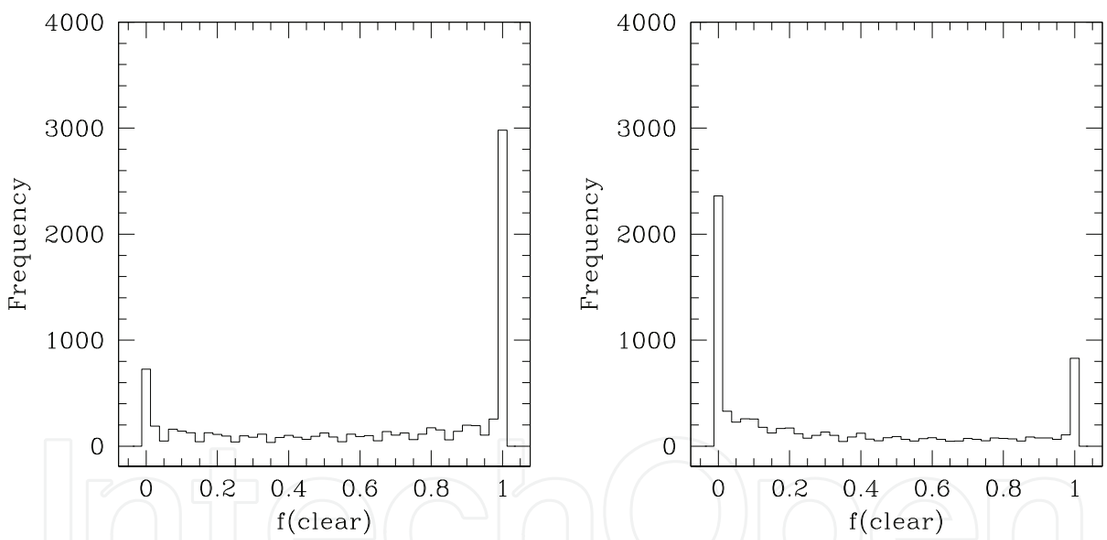

Fig. 8. Distribution of hourly clear fraction for the dry (left) and wet (right) seasons, for Sierra Negra.

The contrast between dry and wet semesters is well illustrated in the left panel of Fig. 9, showing the median and quartile fractions of clear time for successive wet and dry semesters. Semesters are taken continuously, from May to October representing the wet season and November to April of the following year for the dry season. The bars represent the dispersion in the data, measured by the interquartile range. Large fluctuations are observed at any time of the year. The contrast between the clearer dry months, with median daily clear fractions typically above 75 %, and the cloudier wet months, with median clear fractions below 20 %, is evident. The seasonal variation can be seen with more detail in the monthly distribution of the clear weather fraction, combining the data of different years for the same month, shown

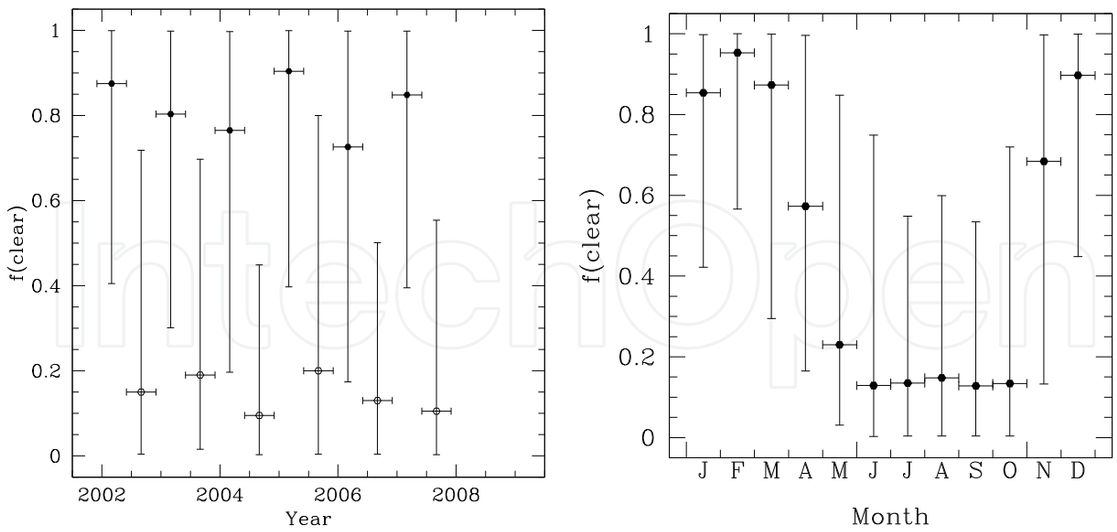

Fig. 9. Left: clear fractions for the different seasons. Points are at median; bars go from 1st to 3rd quartile. Wet season (open dots) is the yearly interval from May to October; dry season (full dots) is from November to April of the following year. Right: the median and quartile values of the fraction of clear weather for the different months of the year.

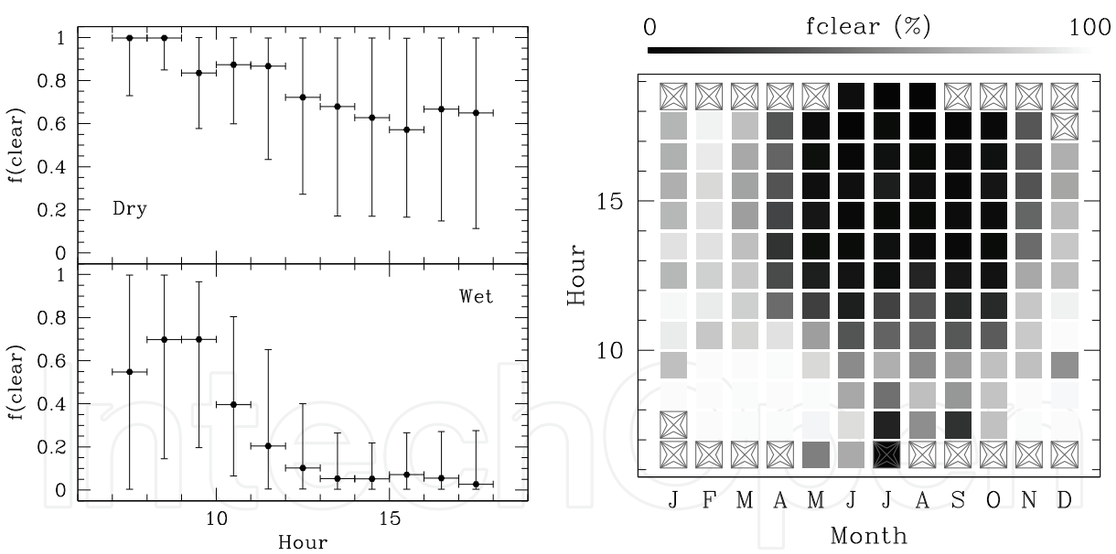

Fig. 10. Left: median and quartile values of the fraction of clear weather fclear, for each hour of day. The lower and upper panels are for wet (MJJASO) and dry (NDJFMA) semesters, respectively. Right: a grey level plot showing the median fraction of clear time f(clear), for each month and hour of day. Squares are drawn when more than 10 h of data are available; crosses indicate less than 10 h of data.

on the right side of the same figure. The skies are clear, f(clear)$>$ 80 %, between December and March, fair in April and November, f(clear)$\sim$ 60 %, and poor between May and October,

f(clear)$<$ 30 %. The fluctuations in the data are such that clear fractions above 55 % can be found 25 % of the time, even in the worst observing months.

Fig. 10 (left) shows the median and quartile clear fractions as function of hour of day for the wet/dry subsets. The interquartile range practically covers the (0-1) interval at most times. We note that good conditions are more common in the mornings of the dry semesters, while the worst conditions prevail in the afternoon of the wet season, dominated by Monsoon rain storms. The trend in our results for daytime is consistent with that obtained by applying different methods (1). By analysing the clear fraction during day and nighttime these authors found that the clear fraction is highest before noon, has a minimum in the afternoon and increases during nighttime.

On the right panel of Fig. 10 a grey level plot of the median percentage of clear time for a given combination of month and hour of day, is shown. Dark squares show cloudy weather, clearly dominant in the afternoons of the rainy months. These are known to be the times of stormy weather in the near-equator. Clear conditions are present in the colder and drier months. This plot is similar to that of humidity. In fact, when relative humidity decreases, the fraction of clear time increases, as shown in Fig. 11.

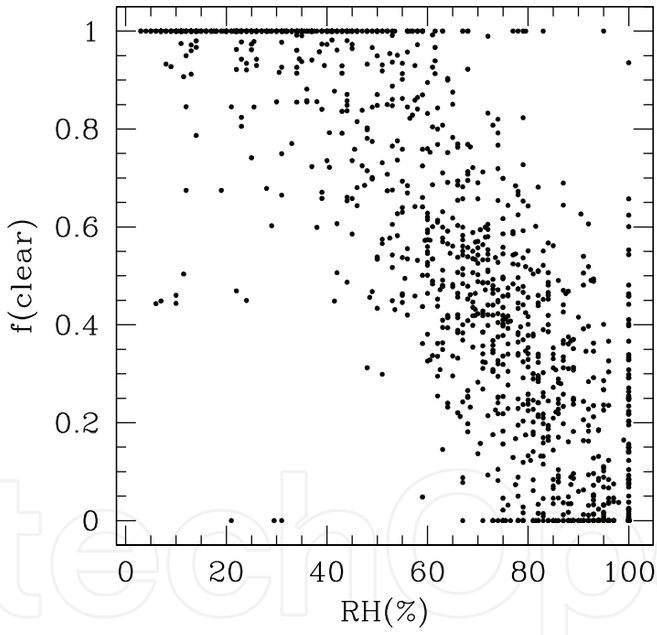

Fig. 11. Relative humidity (RH) vs. fraction of clear time, for Sierra Negra. It is apparent that there is a trend: for low values of RH, f(clear) is larger.

3.5 The histogram of $\psi(t)$ for San Pedro Mártir

The same analysis was carried out for SPM radiation data. The normalized histogram of ψ for all the data is shown in Fig. 12. It presents a double peak in the clear component, not fully consistent with the standard narrow component fit function, and the cloud component with maximum at $\psi \lesssim 0.3$. We applied the double component fit of Eq. 12, shown in the same

figure. The fit for the clear component is drawn in blue, for the cloud component in green and for the sum in red. The coefficients of the fit and associated errors are presented in Table 3. Fit errors were obtained through a bootstrap analysis using 10000 samples. The fit agrees with the data within the statistics, except in the wings of the clear peak. Still, the Lorentzian function proved to fit much better the data than a Gaussian. The fit can be better appreciated in a logarithm version shown on the right side of the same figure.

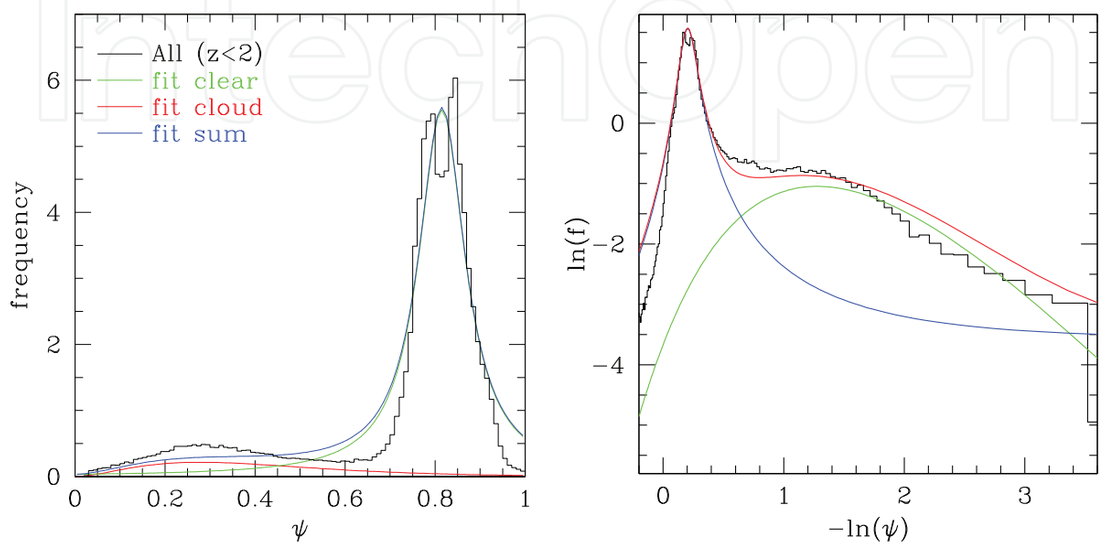

Fig. 12. *Left*: the normalized observed distribution of ψ for all the data and the corresponding fits for SPM. The blue line is the fit to clear weather; the green one to cloudy weather and the red line to the sum. *Right* : the logarithm of the normalized observed distribution of ψ and of the corresponding fits.

Parameter	Global $z < 2$	Bootstrap	errors	relative error (10^{-3})
A	40.8	40.766	$\pm$0.612	15.0
β	7.19	7.175	$\pm$0.044	6.2
B	6.03	6.035	$\pm$0.055	9.1
ψ_0	0.815	0.8151	$\pm$0.0002	0.3
$\Delta\psi$	0.063	0.0629	$\pm$0.0005	7.5
f(clear)	0.824	0.8238	$\pm$0.0009	1.1
f(cloud)	0.176	0.1762	$\pm$0.0009	5.0

Table 3. Parameters of the fit shown in red Fig. 12.

We considered data with $\psi \leq \psi_{min}$, where $\psi_{min} = 0.58$, as cloudy weather and data with $\psi > \psi_{min}$ as clear weather. The value $\psi_{min} = 0.58$ corresponds to the intersection of the two components of the function fitted to the distribution of all data points. As mentioned, the fraction of clear time f(clear), was computed as clear/(clear+cloudy). From the global histogram we obtained for SPM a clear fraction for the site of 82.4 %. The errors in the determination of f(clear) and f(cloud), were also obtained by generating 10000 bootstrap samples; they are shown in Table 3.

The 82.4 % of clear fraction obtained from the global distribution shown in Fig. 12 is similar to that reported using satellite data (1). These authors estimated that the usable fractions of nightime at SPM was 81 %. Their definition of usable time includes conditions with high cirrus. For the case of SPM, they conclude that the day versus night variation of cloud cover is less than 5 %, being clearer at night. Therefore, the results presented here are consistent within 6.4 % with those reported in the literature (1).

Another estimation of the useful observing time at SPM by Tapia (10) reports a 20 yr statistics of the fractional number of nights with totally clear, partially clear and mostly cloudy based in the observing log file of the 2.1m telescope night assistants. The author reports a total fraction of useful observing time of 80.8 % and compares his results with those from other authors (1); he concludes that the monthly results from both studies agree within 5 % while for the yearly fraction, the discrepancies are lower than 2.5 %. Therefore, our results in this case, are also consistent with those obtained with completely different techniques.

Futhermore, when analyzing the fits per month we realized that the Lorentzian fits for the clear weather peak were better than that of the complete dataset: to study the seasonal variation of ψ we created histograms and the corresponding fits per month. Consider the histogram and corresponding fit for July and November shown Fig. 13. It can be appreciated that the fits reproduce the distribution of ψ very well. The narrow clear component is consistent with prevailing clear sky conditions, for which the solar radiation reaches the site with only the attenuation of the atmosphere. The coefficients of the fits presented in Fig. 13, according to the functional form of $f(\psi)$, Eq. 12, are shown in Table 4. The fits can be better valued in the logarithm displays of Fig. 13, presented in Fig. 14. The fits to the complete data (red line), to clear weather (blue line) and to cloudy weather (green line) are indicated.

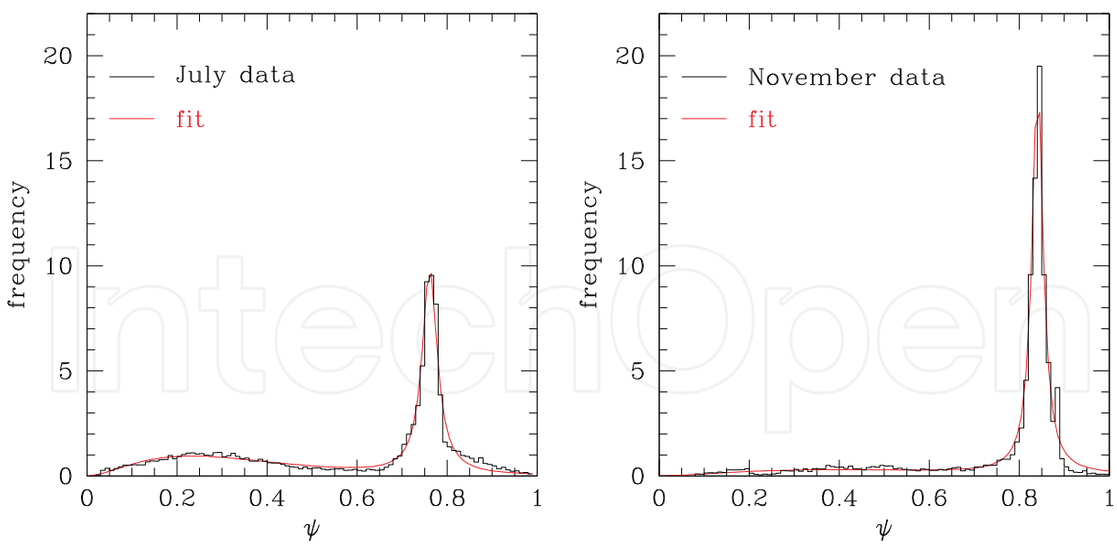

Fig. 13. The observed distribution of ψ and the two component fit for July (*left)* and November (*right)*. Comparing both plots a shift in the centre of the narrow component is clearly appreciated.

We studied the position of the centre of the peak corresponding to the clear fraction as a function of the month of each observed year. We found that for every year there is a cyclic

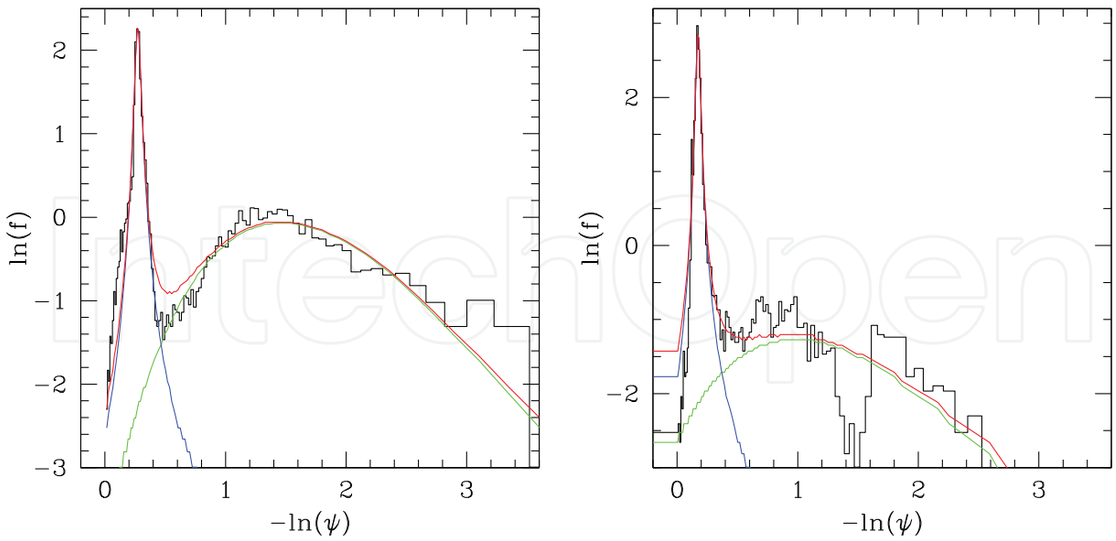

Fig. 14. The logarithm plots of the observed distribution of ψ for July (*left)* and November (*right)* shown in Fig. 13. Note that even in the case of low statistics the fit proves to be good.

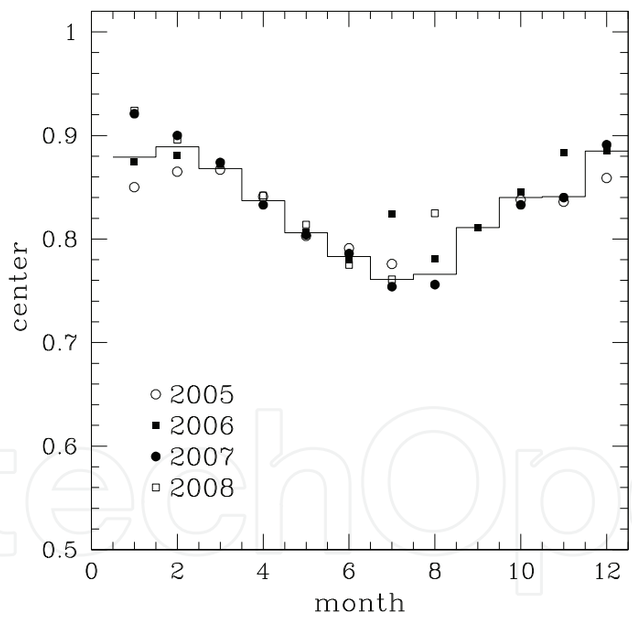

Fig. 15. The centre of the narrow component of ψ for each month. The monthly values for all the data are indicated by the histogram, while the dots mark individual months of different years. The position of the narrow peak component is not constant during the year, reaching a minimum in July. The error bars are smaller than the symbols.

effect: the centre of the peak is 0.880 in January, reaches a maximum around 0.889 in February, decreases to a minimum of 0.761 in July and increases towards the end of the year to 0.885 in

Sample	A	β	B	ψ_0	$\Delta\psi_0$
July	135.2	8.68	9.24	0.761	0.021
	$\pm$1.5	$\pm$0.112	$\pm$0.141	$\pm$0.0005	$\pm$0.001
November	11.7	3.83	19.07	0.841	0.015
	$\pm$2.6	$\pm$0.189	$\pm$0.236	$\pm$0.0009	$\pm$0.002

Table 4. Coefficients of the fits shown in Fig. 13.

December. Errors in the statistical determination of ψ_0 are $\lesssim 0.001$. Fig. 15 shows the position of the centre of the narrow component obtained using the whole data set for each month with a solid line. The corresponding values of the individual months for different years are indicated by distinct symbols.

The solar radiation sensor accuracy is $\pm$5 %. However, considering N ($\sim$20000) data points per bin, the position of the peaks are statistical variables determined with an accuracy $\propto 1/\sqrt{N}$ times the individual measurement error i.e. much better than 5 %. Hence, the variations in the position of the centres observed with an amplitude of up to 14 % are statistically robust. Still, the amount of radiation corresponding to the clear peak in July is higher by 277 Wm^{-2} than that received in November.

The variation trend in the centre of the clear peak shown in Fig. 15 can be interpreted in terms of seasonal variations of the atmospheric transmission: there are more aerosols during spring (maximum) and summer than in the rest of the year (6). This is also consistent with the seasonal variation of the Precipitable Water Vapor (PWV) at 210 GHz reported by different authors (11), (12), (13; 14), as the maximum PWV values occur during the Summer. From these results we concluded that the double peak in the global distribution of ψ is a real effect due to absorption variations in the atmosphere.

The larger value of the centers of the clear peak for July 2006 and August 2008 relative to the same months of the other years, shown in Fig. 15, suggest that the atmosphere was more transparent. We analyzed the aerosol optical thickness reported by (6). The larger value of the centre for July 2006 is consistent with smaller values of the aerosol optical thickness for July 2005 and 2007 but marginally for July 2008. The bigger value of the centre for August 2008 is also consistent with smaller values of the aerosol optical depth for August 2007 and marginally for August 2006 while for August 2005 there is not data available.

3.6 Statistics of clear time for SPM

First, the fraction of clear time obtained for every hour of data, accumulating 7828 h is shown in Fig. 16. We note that it behaves in a rather unimodal fashion: 78.6 % have $f(\mathrm{clear}) = 1$ while 9.5 % of the hours have $f(\mathrm{clear}) = 0$. The remaining fraction of data (12.5%) have intermediate values.

The solar radiation data observed at airmass lower than 2 is a subset of that observed below 10. For completeness, in this analysis we considered data with airmass less than 10.

The contrast between summer and the other seasons is well illustrated on the right side of Fig. 16, showing the median and quartile fractions of clear time for successive years. The bars represent the dispersion in the data measured by the interquartile range. The quartiles are indicative of the fluctuations and therefore more representative than averages. Large variations are observed mainly during the summer months for the whole period.

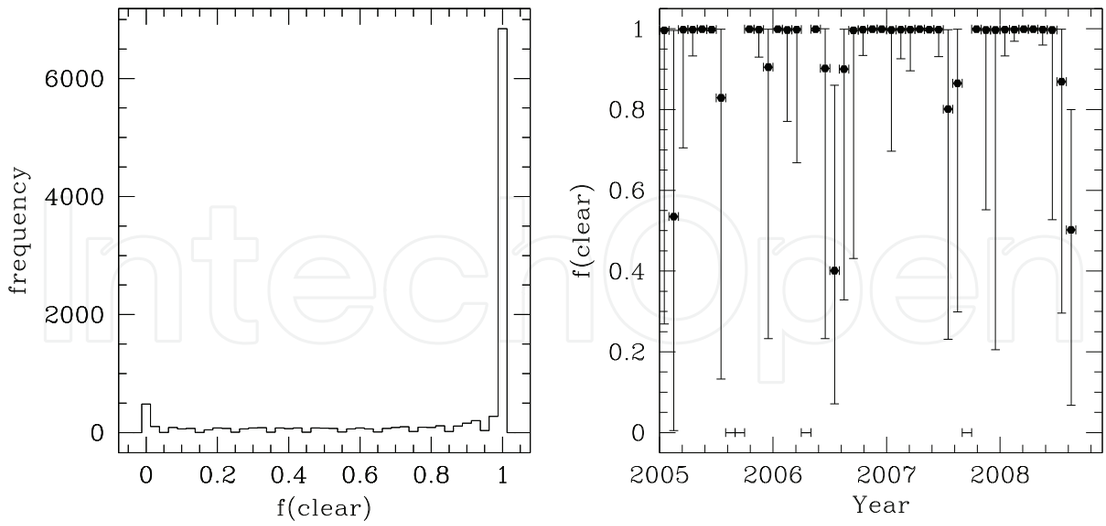

Fig. 16. Left: distribution of hourly clear fraction for the 7828 datapoints available. Right: clear fractions for the different months. Points are at median; bars go from 1st to 3rd quartile. The annual cycle can be appreciated.

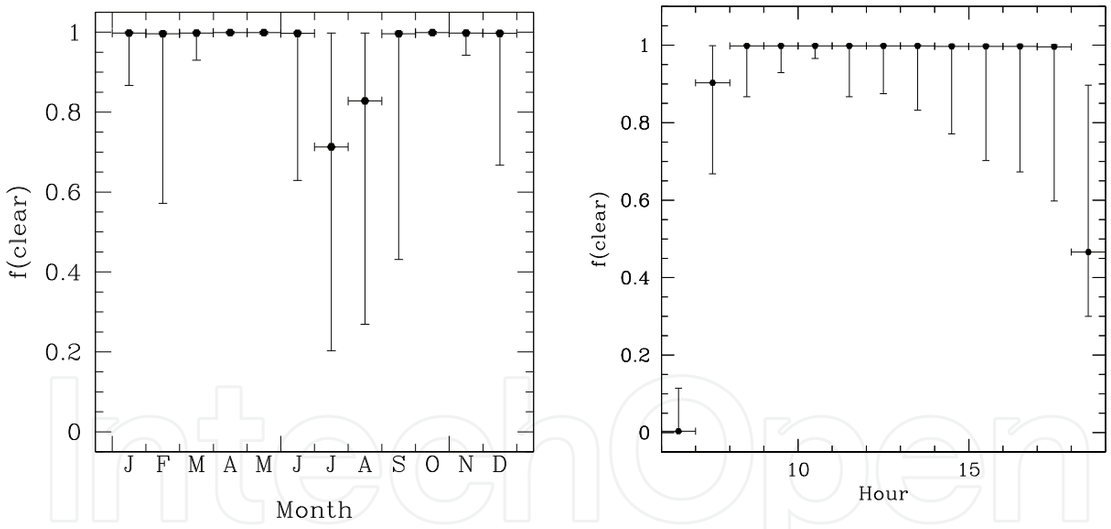

Fig. 17. Left: median and quartile values of the monthly clear fraction. Right: median and quartile values of the hourly clear fraction

Considerable fluctuations are also present for 2005 in January, February and December. The latter is not reproduced in 2006 but in 2007 there is also a large fluctuation in December. The contrast between the spring and autumn months, with median daily clear fractions typically above 98 %, and the cloudier months with median clear fractions below 80 % is evident.

The seasonal variation can be seen with more detail in the monthly distribution of the clear weather fraction, combining the data of different years for the same month, shown on the

left side of Fig. 17. The skies are clear, f(clear)$>$ 99 %, between March and May, relatively poor between June and September with a minimum median value of f(clear)$<$ 72 % and fair between December and February when in the worst case 25 % of the time f(clear)$<$ 57 %.

The right side of Fig. 17 shows the median and quartile clear fractions as function of hour of day. Good conditions are more common in the mornings. The trend in our results for daytime is consistent with that obtained by (1). By analysing the clear fraction during day and nighttime they found that the clear fraction is highest before noon, has a minimum in the afternoon and increases during nighttime. The authors associated the afternoon maximum in cloudiness with lifting of the inversion and cloud layer because the site is high enough to be located above the inversion layer at night and in the mornings.

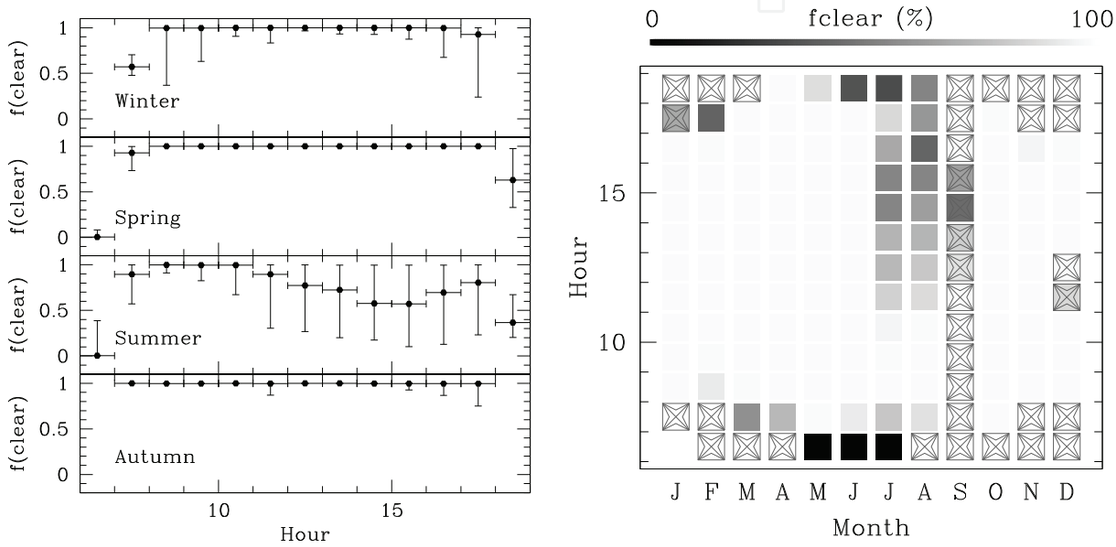

Fig. 18. Left: graph showing the median and quartile values of the fraction of clear weather for each hour of day for each season. Right: a grey level plot showing the median fraction of clear time f(clear), for each month and hour of day. Squares are drawn when more than 10 h of data are available; crosses indicate less than 10 h of data.

The left panel of Fig. 18 presents the median and quartiles of clear fraction as a function of hour of day for the seasons subsets. Seasons were considered as follows, winter: January, February and March; spring: Abril, May and June; summer: July, August and September and autumn: October, November and December. It is clear that during the summer the conditions are more variable than at any other epoch of the year. In the other seasons the conditions are very stable.

The right side of Fig. 18 shows a grey level plot of the median percentage of clear time for a given combination of month and hour of day. Squares are drawn when more than 10 h of data are available; crosses indicate less than 10 h of data. Clear conditions are present in the colder and drier months, from October to June. Dark squares show cloudy weather, clearly dominant in the afternoons of the summer months, from July to September.

We repeated the analysis for airmass lower than 2. An equivalent histogram to that shown in Fig. 16, was created by computing the fraction of f(clear) for every hour, adding 5211 h. As expected, it also has an almost unimodal distribution: 82.5 % have f(clear) = 1 while 6.7 %

of hours f(clear) = 0. The remaining fraction of data have intermediate values. The values of f(clear) obtained for the periodicities presented in this section are very similar but with less dispersion. In fact, in the analysis per hour the difference in median values are within 0.1 %. For the analysis per month the differences are also in that range except for July and August with differences between 0.3 to 13 %, with a maximum of 20 % for July 2006. The lower values obtained for the global distribution and for different periods can be explained by the presence of clouds formed at airmass $2 < z < 10$. The equivalent grey level plot of Fig. 18 for airmass less than 2 (not shown) does not include the contribution of clouds formed in the early morning and late afternoon hours, specially during the summer months.

3.7 Summary

We have presented a method to estimate the temporal fraction of cloud cover based on calculating the ratio between the expected amount of radiation and that observed. We described the equations to compute the solar modulation given the latitude of the site under study. These equations were applied to two different sites: Sierra Negra, at $b \simeq 19^\circ$ located three degrees south of the tropic of Cancer and San Pedro Mártir, located in the Baja California at $b \simeq 31^\circ$N. Knowing the position of the Sun at the site as a function of time, we computed the variable ψ, given by $\psi(t) = F(t)/s_\odot \cos\theta_\odot$, where F(t) is the solar flux measured and $s_\odot \cos\theta_\odot(t)$ is the nominal solar flux at the top of the atmosphere. From the global normalized observed distribution of ψ, we calculated the fraction of time when the sky is clear of clouds.

The fit to the histograms of ψ developed for Sierra Negra (2) also reproduced the SPM data (3), showing that this method might be generalized to other sites. Furthermore, the consistency of our results with those obtained by other authors shows the great potential of our method as cloud cover is a crucial parameter for characterization of any site and can be estimated from i*in situ* measurements.

4. Acknowledgments

The authors acknowledge the kindness of the TMT site-testing group. The authors specially thank G. Sanders, G. Djorgovski, A. Walker and M. Schöck for their permission to use the results from the report by Erasmus & Van Staden (1) for Sierra Negra and SPM. The authors also thank Jorge Reyes for his help with the images.

5. Apendix: fit and errors

The radiation flux $F(t)$ is normalized to a function $\psi = F(t)/s_\odot \cos\theta_\odot(t)$. The observed distribution of ψ is well fitted by the function

$$f(x) = Ax^2 e^{-\beta x} + \frac{B}{1 + ((x - x_0)/\Delta x)^2}.$$

- The first term on the right hand side is a χ^2 function with six degrees of freedom. The function has maximum at $x_{max} = 2/\beta \simeq 0.28$ for our data. It is interpreted as the "cloud-cover" part of the data, with its integral over the unitary interval,

$$\int_0^1 Ax^2 e^{-\beta x} dx = \frac{2A}{\beta^3}\left[1 - \left(1 + \beta + \beta^2/2\right) e^{-\beta}\right]$$
$$\rightarrow 2A/\beta^3 \quad \text{for} \quad \beta \gg 1,$$

the fraction of "cloud-covered" time. For the SPM($z < 2$) sample we have $A = 40.8, \beta = 7.19$ and $2A/\beta^3 \left[1 - \left(1 + \beta + \beta^2/2\right) e^{-\beta}\right] = 0.2195(0.974) = 0.2139$. The correct unitary normalization is for

$$A^* = \frac{\beta^3/2}{1 - (1 + \beta + \beta^2/2)e^{-\beta}} = 189.74.$$

- The second term, a Lorentzian function of center x_0 and width Δx, represents the "cloud-clear" part of the data. The fitting function is normalized around x_0 such that

$$\int_{x_0-\eta_0\Delta x}^{x_0+\eta_1\Delta x} \frac{B\,dx}{1 + (x - x_0/\Delta x)^2} = B\Delta x\,(\arctan(\eta_1) + \arctan(\eta_0)) \rightarrow B\pi\Delta x \quad \text{for} \quad \eta_{0,1} \gg 1,$$

the term $B\Delta x(\arctan(\eta_1) + \arctan(\eta_0))$ represents the "clear" fraction. For the SPM($z < 2$) data $B = 6.03$, $x_0 = 0.8151$, $\Delta x = 0.063$, I take $\eta_0 = x_0/\Delta x = 12.938$ and $\eta_1 = (1 - x_0)/\Delta x = 2.935$ so $\arctan\eta_1 + \arctan\eta_0 = 0.8709\pi$ and the correct normalization factor should be $B^* = 5.801$.

The fit requires determining the five parameters through residual minimization. The determination of $\{\beta, x_0, \Delta x\}$, determining the shape of the distribution, is numerical; that of A, B is analytical through solving

$$\left\langle yx^2e^{-\beta x} \right\rangle = A \left\langle \left(x^2e^{-\beta x}\right)^2 \right\rangle + B \left\langle \frac{x^2e^{-\beta x}}{1 + ((x - x_0)/\Delta x)^2} \right\rangle$$

$$\left\langle \frac{y}{1 + ((x - x_0)/\Delta x)^2} \right\rangle = A \left\langle \frac{x^2e^{-\beta x}}{1 + ((x - x_0)/\Delta x)^2} \right\rangle + B \left\langle \left(\frac{1}{1 + ((x - x_0)/\Delta x)^2}\right)^2 \right\rangle$$

Strictly speaking, we should have $A = (1 - w)A^*$ and $B = wB^*$ with w defining the "clear fraction".

Error determination can, in principle, be done with the process of residual minimization, through a parabolic fit to the function describing the figure of merit. Given the nature of the fitting functions this is not practical; we proceeded through a bootstrap analysis of the $(z < 2)$ sample containing $N \simeq 180,000$ points, obtaining the results shown in tables 3 and 4. To determine the errors in subsamples of size N_s we assume errors scale as $\sqrt{N/N_s}$.

6. References

[1] Erasmus A, & Van Staden C. A., 2002, "A satellite survey of cloud cover and water vapor in the western USA and Northen Mexico. A study conducted for the CELT project.", internal report

[2] Carrasco, E., Carramiñana, A., Avila, A., Guitérrez, C., Avilés, J.L., Reyes, J., Meza, J. & Yam, O., (2009), *MNRAS*, 398, 407

[3] Carrasco, E., Carramiñana, A., Sánchez, L. J., Avila, R. & Cruz-González, I., (2012), *MNRAS*, 420, 1273-1280

[4] http://mips.as.arizona.edu/∼cnaw/sun.html

[5] Tapia M., Hiriart D., Richer M. & Cruz-González, I.,(2007), Rev. Mex. AA (SC), 31, 47

[6] Araiza M.R. & Cruz-González I., (2011) Rev. Mex. AA 47, 409

[7] Cruz-González I., Avila R. & Tapia M., eds, (2003), Rev. Mex. AA (SC), 19.
[8] Cruz-González I., Echevarría J. & Hiriart D., eds, (2007), Rev. Mex. AA (SC), 31
[9] Schöck M. et al., (2009), Publ. Astr. Soc. Pac., 121, 384
[10] Tapia M., (2003), Rev. Mex. AA (SC), 19, 75
[11] Hiriart D. et al., (1997), Rev. Mex. AA, 33, 59
[12] Hiriart D. et al., (2003), Rev. Mex. AA (SC), 19, 90
[13] Otárola A. et al., (2009), Rev. Mex. AA, 45, 161
[14] Otárola A. et al., (2010), Publ. Astr. Soc. Pac., 122, 470

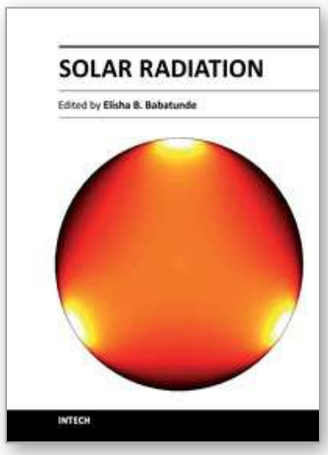

Solar Radiation

Edited by Prof. Elisha B. Babatunde

ISBN 978-953-51-0384-4
Hard cover, 484 pages
Publisher InTech
Published online 21, March, 2012
Published in print edition March, 2012

The book contains fundamentals of solar radiation, its ecological impacts, applications, especially in agriculture, architecture, thermal and electric energy. Chapters are written by numerous experienced scientists in the field from various parts of the world. Apart from chapter one which is the introductory chapter of the book, that gives a general topic insight of the book, there are 24 more chapters that cover various fields of solar radiation. These fields include: Measurements and Analysis of Solar Radiation, Agricultural Application / Bio-effect, Architectural Application, Electricity Generation Application and Thermal Energy Application. This book aims to provide a clear scientific insight on Solar Radiation to scientist and students.

InTech Europe
University Campus STeP Ri
Slavka Krautzeka 83/A
51000 Rijeka, Croatia
Phone: +385 (51) 770 447
Fax: +385 (51) 686 166
www.intechopen.com

InTech China
Unit 405, Office Block, Hotel Equatorial Shanghai
No.65, Yan An Road (West), Shanghai, 200040, China
中国上海市延安西路65号上海国际贵都大饭店办公楼405单元
Phone: +86-21-62489820
Fax: +86-21-62489821

IntechOpen